Electronic Supplementary Information

Structure-Dependent Mechanism of Single-atom Cobalt on Macroporous Carbon Nitride in (Photo-)Fenton-Like Reaction

Jingkai Lin,[a] Lin Jiang,[a] Wenjie Tian,[a] Yangyang Yang,[a] Xiaoguang Duan,[a] Yan Jiao,[a*] Huayang Zhang,[a*] and Shaobin Wang[a*]

a School of Chemical Engineering, The University of Adelaide, North Terrace, Adelaide, SA 5005, Australia;

E-mail: huayang.zhang@adelaide.edu.au; yan.jiao@adelaide.edu.au; shaobin.wang@adelaide.edu.au

1. Experimental Procedures

Fabrication of macroporous carbon nitride (MCN)

MCN was prepared following the similar preparation process without the addition of metal precursors. Specifically, DCD was uniformly tiled on the surface of silica templates for calcination (520 °C with a ramp of 2 °C·min^{-1} for 2 h and further to 550 °C with a ramp of 4 °C min^{-1} for 2 h, nitrogen gas). The resulting product was etched with 4 M NH_4HF_2 aqueous solution (50 mL) for 48 h for the removal of silica template completely. After that, the as-obtained solid was washed with ultrapure water several times and dried at 60 °C overnight. The collected sample was labelled as MCN.

Fabrication of pure carbon nitride (CN)

Bulk carbon nitride was prepared by directly calcining DCD under nitrogen gas at 520 °C with a ramp of 2 °C·min^{-1} for 2 h and further to 550 °C with a ramp of 4 °C min^{-1} for 2 h. After that, the as-obtained solid was washed with ultrapure water several times and dried at 60 °C overnight. The sample was then labelled as CN.

Quenching experiments

All quenching reagents were added to the BPA solution (10 ppm) before the addition of catalyst (0.2 g/L) and PMS (0.5 mM). Methanol (MeOH, 100, 200, and 500 mM) was added as the radical scavenger for both •OH and $SO_4^{\bullet-}$ (k_1 (•OH, MeOH) = 1.6 - 7.7 × 10^7 M^{-1} s^{-1}, k_2($SO_4^{\bullet-}$, MeOH) = 1.2 - 2.8 × 109 M^{-1} s^{-1}). Tert-butanol (TBA, 100, 200, and 500 mM) was added as the radical scavenger for •OH (k_1 (•OH, TBA) = 6.0 × 10^8 M^{-1} s^{-1}). p-benzoquinone (p-BQ, 0.5, 1 and 2 mM) was added as the radical scavenger for superoxide radicals ($O_2^{\bullet-}$, k_1 ($O_2^{\bullet-}$, p-BQ) = 0.9 – 1.0 × 10^9 M^{-1} s^{-1}). Furfuryl alcohol (FFA, 0.5, 1 and 2 mM) and 2,2,6,6,-tetramethyl-4-piperidinol (TEMP, 1 mM) were added as the quenching agent for $^1O_2$ (($^1O_2$, FFA) = 1.2 × 10^8 M^{-1} s^{-1}). *di*-Ammonium oxalate monohydrate (AMO, 2 mM) was added as the quenching agent for holes. Methyl phenyl sulfoxide (PMSO, 1 mM) was added to investigate the effect of high-valent cobalt species. In the study of the effect of molecular oxygen on BPA degradation, the reaction solution was bubbled by N_2 for 30 min before the reaction started, and continuing purging during the reaction.

Activity evaluation of different organic pollutants

For the HPLC operation with other organic pollutants, the mobile phase was changed.

Phenol: Acetonitrile (30%) and ultrapure water (70%) were applied as the mobile phase at a flow rate of 1.0 mL min^{-1}.

Sulfamethoxazole (SMX): Acetonitrile (50%) and ultrapure water (50%) were applied as the mobile phase at a flow rate of 1.0 mL min^{-1}.

p-Hydroxybenzoic acid (HBA): Acetic acid (60%) and methanol (40%) were applied as the mobile phase at a flow rate of 1.0 mL min^{-1}.

Naproxen (NPX): Acetic acid (20%), methanol (70%) and ultrapure water (10%) were applied as the mobile phase at a flow rate of 1.0 mL min^{-1}.

Acyclovir (ACV): Methanol (7%) and ultrapure water (93%) were applied as the mobile phase at a flow rate of 1.0 mL min^{-1}.

Studies of pH effect

The pH of initial BPA solution was adjusted to a certain value (pH=5, 9, 11) using 0.1 M hydrochloric acid and sodium hydroxide before adding catalysts and PMS.

Cycling tests

The catalyst after each run was reclaimed and dissolved in 50% ethanol solution and ultrasonic washed for 1 h. After that, the samples were washed with ultrapure water. The collected samples were dried at 60 ^{o}C for the next round.

PMS adsorption evaluation

The PMS adsorption evaluation was performed using an iodometric method to analyze the concentration of PMS in reaction solution. In detail, 20 mg catalysts were dispersed in 100 mL PMS solution (0.5 mM) at 25 ^{o}C with constant stirring. Reaction solution was withdrawn and filtered at 5, 10, 20, 30, 40, 50 and 60 min. A 0.2 mL reaction solution was added to a mixed solution (0.3 g KI, 0.06 g $NaHCO_3$, and 2.8 mL H_2O). The PMS concentration was detected by a UV–vis spectrophotometer at 319 nm (Agilent Technologies, Cary Series).

Theoretical calculation methodology

The simulations of electronic structures were performed by spin-polarized density functional theory (DFT) as implemented in the Vienna Ab Initio Simulation Package (VASP) code.[1–4] The Perdew-Burke-Ernzerhof (PBE) exchange correlation functional of the generalized gradient approximation (GGA) was employed to describe the electron interactions,[5,6] and the projector augmented wave (PAW) pseudopotential was used to describe core electrons, and with plane-wave cutoff energy of 400 eV through all the simulations.[7] An implicit solvation model was applied for all DFT calculations using VASPsol, which implicitly involves counter charges in the system by solving the linearized Poisson-Boltzmann, solvent dielectric constant of 78.4 was set.[8,9] Gaussian smearing approach with a width of 0.05eV was used.[10] The convergence criteria for electronic self-consistent iteration were limited to 1.0×10^{-5} eV, and the ionic relaxation was set to 0.02 eV $Å^{-1}$. The van der Waals interaction has been applied using the DFT-D_3 scheme.[11,12] The vacuum space of 15 Å in z-direction was applied to prevent the interactions between periodic images. Brillouin zone was sampled with a $2 \times 2 \times 1$ k-points using the Monkhorst-Pack scheme grid for geometry optimization, and all the atoms were fully relaxed with self-consistent calculations.[13] The charge transfer analysis of related adsorption configurations is computed by calculating the Bader charge in the chemical species at the gaseous phase, and adsorbed phase.

The adsorption energy (E_{ads}) for PMS is obtained via Eq. S1:

$$E_{ads} = E_{catalysts+PMS} - E_{catalysts} - E_{PMS} \qquad Eq.S1$$

The change of Gibbs free energy (ΔG) for every adsorbed intermediate in this work is thermodynamically corrected via Eq. S2 by considering the vibrational effect.

$$\Delta G = \Delta E_{DFT} + \Delta E_{ZPE} - T\Delta S_{vib} \qquad Eq.S2$$

Where, ΔE_{DFT} represents the reaction energy that is derived directly from VASP computation; ΔE_{ZPE} and ΔS are the differences in zero-point energy and entropy correction corresponding to a desired temperature (25 °C is used in this work) from frequency analysis.

Reaction mechanism for nonradical and radical pathways

The related reaction mechanisms for radical and nonradical generation from PMS (HSO_5) activation were shown in Eqs. S3 - 14 below:[14–17] (* represents adsorption of the intermediates on catalytic Co sites).

$$MCN/Co-N_4 + HSO_5 + * \rightarrow MCN/Co-N_4 + HSO_5^* \qquad Eq.S3$$

$$HSO_5^* \rightarrow {}^*OH + SO_4^* \qquad Eq.S4$$

$${}^*OH + SO_4^* + 2e^- \rightarrow {}^*OH + * + SO_4^{2-} \qquad Eq.S5$$

$${}^*OH + {}^*OH \rightarrow 2{}^*OH \qquad Eq.S6$$

$$2{}^*OH \rightarrow O^* + H_2O \qquad Eq.S7$$

$$O^* + O^* \rightarrow O^*O^* \qquad Eq.S8$$

$$O^*O^* \rightarrow * + {}^1O_2 \qquad Eq.S9$$

$${}^*OH \rightarrow {}^* + \bullet OH \qquad Eq.S10$$

$$HSO_5^* \rightarrow {}^*OOH + SO_3^* \qquad Eq.S11$$

$${}^*OOH + SO_3^* + 2e^- \rightarrow {}^*OOH + * + SO_3^{2-} \qquad Eq.S12$$

$${}^*OOH \rightarrow H^+ + OO^{*-} \qquad Eq.S13$$

$$OO^{*-} \rightarrow * + O_2^{\bullet -} \qquad Eq.S14$$

Corresponding structures of reaction intermediates for the proposed reaction process were constructed and optimized by the DFT computations (**Theoretical methodology** section). Gibbs free energy (ΔG) was calculated for the reaction intermediates.

2. Supplementary Figures

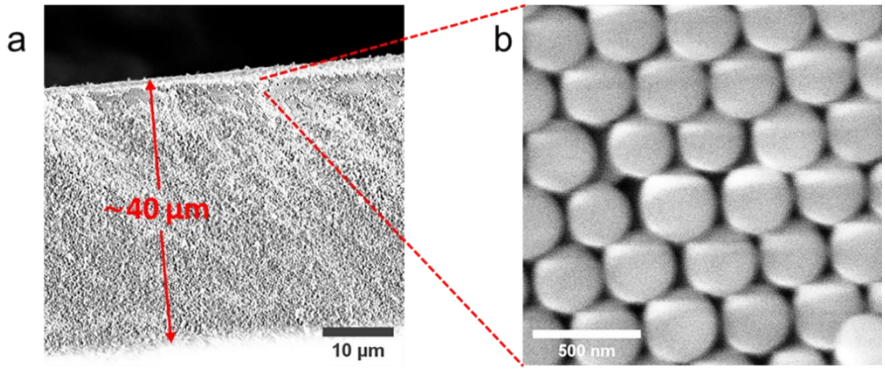

Fig. S1 Cross section SEM images of silica templates (~300 nm in diameter) at a scale of (a) 10 µm (b) 500 nm.

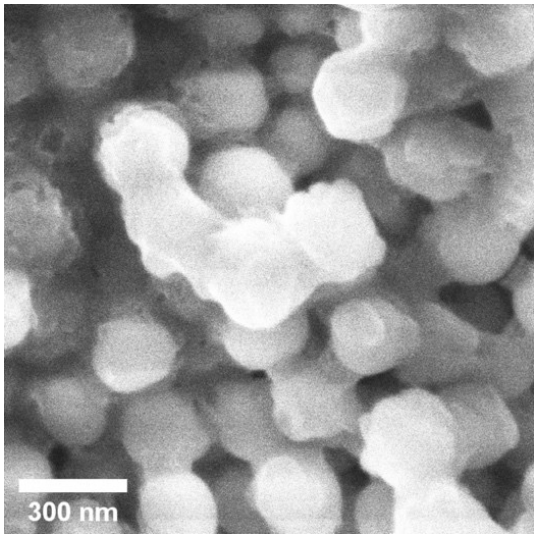

Fig. S2 SEM image of precursors and silica templates after pyrolysis.

The template strips consisting of well-stacked silica nanoparticles were first fabricated by a Stöber strategy, followed by a vertical settlement method.[18] Then, a mixture of $Co(acac)_2$ and DCD was uniformly tiled on the surface of silica templates, which would melt and fill into the gaps between adjacent silica spheres during the subsequent stepwise heat treatment (520 °C/2 h → 550 °C/2 h). The precursors were confined in between the gap of adjacent silica spheres, facilitating the immobilization of single-atom Co between melon polymer chains (Fig. S4).

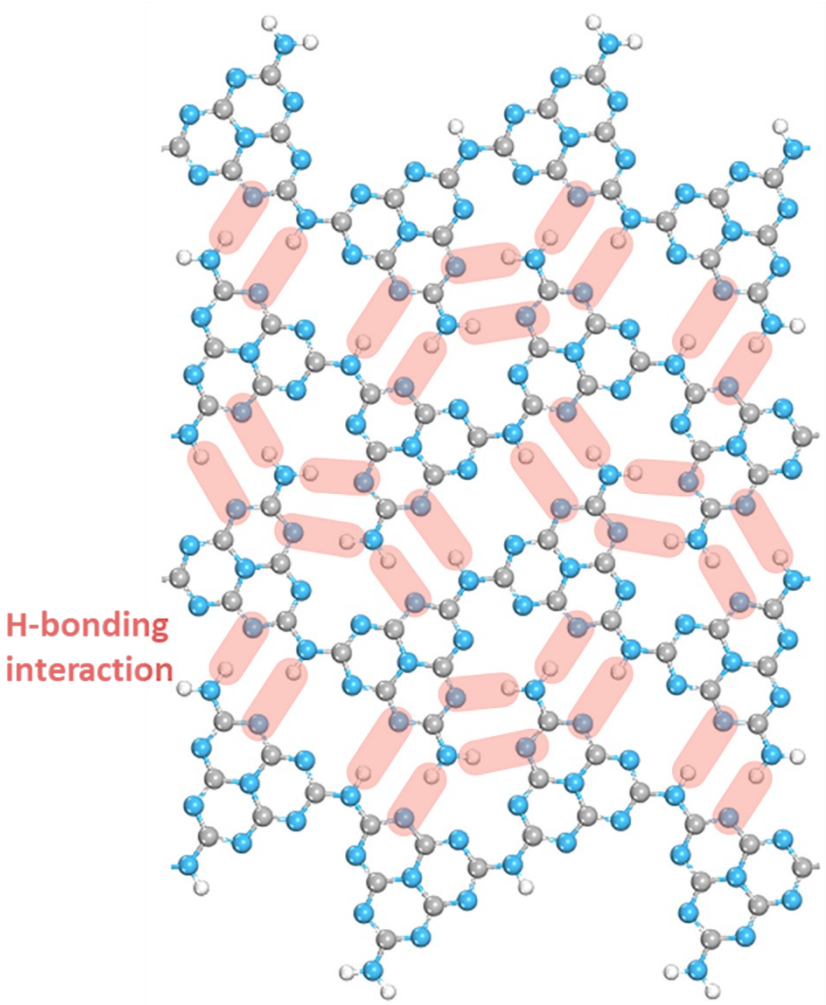

Fig. S3 Structure models of carbon nitride: Hydrogen-bonded melon chains.

Carbon nitride derived from the thermal condensation of DCD possesses hydrogen-bonded polymeric melon structures with NH/NH_2 groups.[19,20]

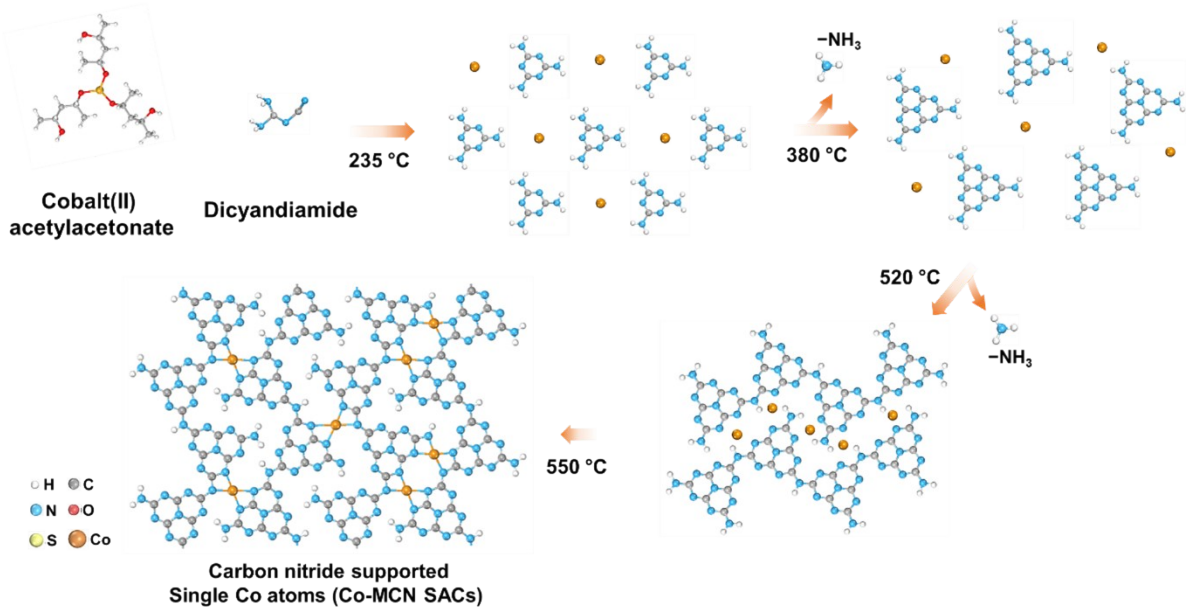

Fig. S4 Proposed formation route of carbon nitride-supported Co single atoms (Co-MCN SACs).

DCD is gradually pyrolyzed to form melamine (> 235 °C), melem (> 380 °C), melon (> 510 °C), and finally graphitic carbon nitride (> 550 °C).[21] The temperature holding at 520 °C for 2 h benefited the coordination of Co atoms with melon polymer chains. The structure was further stabilized at 550 °C, allowing the formation of a maximum amount of NH and NH_2 surface functional groups for anchoring Co single atoms.[22]

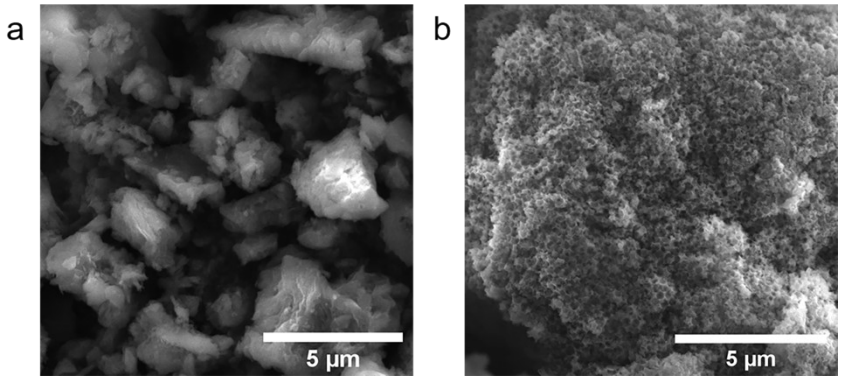

Fig. S5 SEM images of (a) CN and (b) MCN.

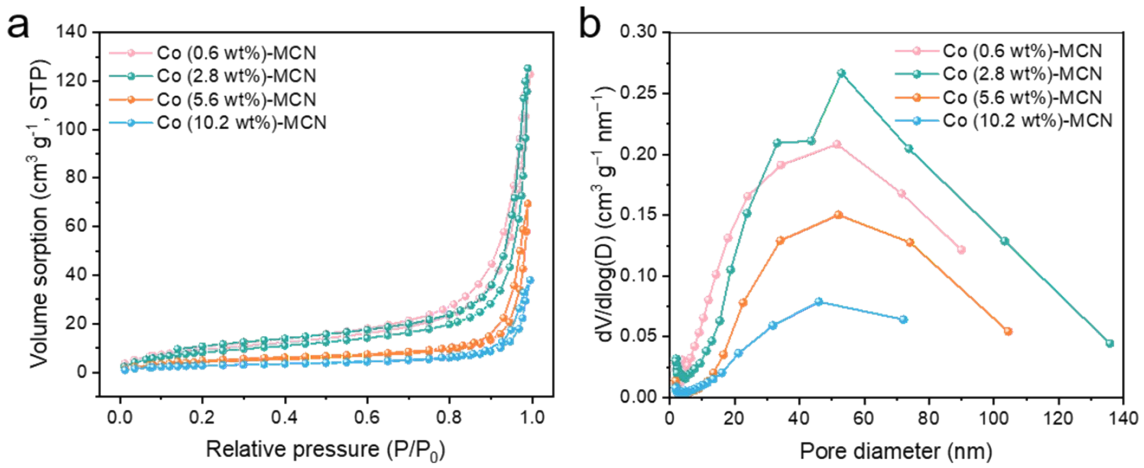

Fig. S6 (a) N_2 sorption isotherms and (b) Barret-Joyner-Halender (BJH) pore size distribution curves of Co-MCN SACs.

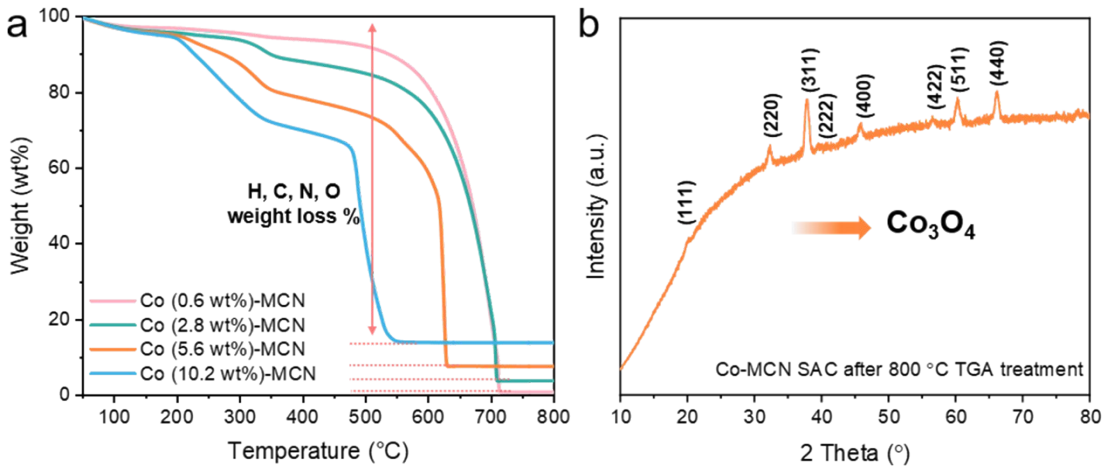

Fig. S7 (a) TGA curves of Co-MCN SACs, (b) formation of Co_3O_4 confirmed by XRD patterns.

The weighting percentage of single-atom Co in Co-MCN SACs was determined by the thermogravimetric analysis (TGA, Fig. S7a).[23] Initial weight (w. initial) of a sample was first recorded. After pyrolysis to 800 °C, the remaining weight of the sample was recorded (w. remaining, which has been subtracted with the weight change of crucible, 0.61 mg at 800 °C). The sample weight loss is only contributed to the loss of H, C, N, O. In an air flow, Co is oxidized into Co_3O_4 (Fig. S7b). The remaining weight was accepted as the weight of Co_3O_4 in the crucible. Considering the atomic mass of Co_3O_4 (240.8 g mol^{-1}; Co: 58.9 g mol^{-1}, O: 16 g mol^{-1}, the mole percentage of Co in Co_3O_4 can then be determined as 73.4%), and the weight of Co atoms in the as-produced Co_3O_4 can be calculated (Eq. S15), which is consistent with the weight of Co single atoms in the initial sample. Finally, the weighting percentage of Co single atoms was calculated by dividing the weight of Co by the initial weight of the catalyst.

$$Co\ wt\% = \frac{73.4\% \cdot w.remaining}{w.intital} \qquad Eq.S15$$

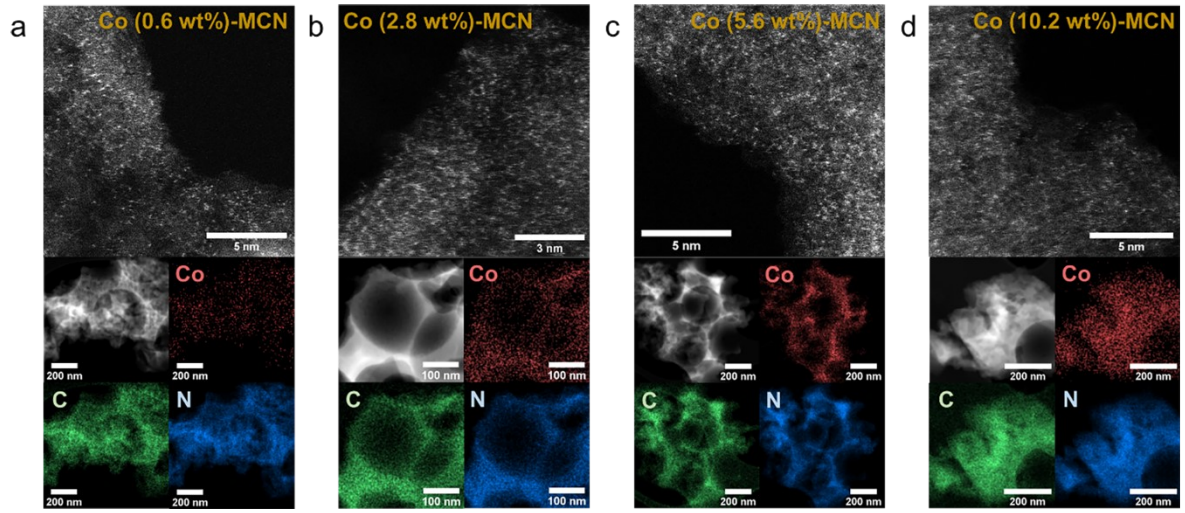

Fig. S8 AC-HAADF-STEM images, HAADF-STEM images and energy dispersive spectrometer (EDS) elemental mappings of (a) Co (0.6 wt%)-MCN, (b) Co (2.8 wt%)-MCN, (c) Co (5.6 wt%)-MCN, and (d) Co (10.2 wt%)-MCN.

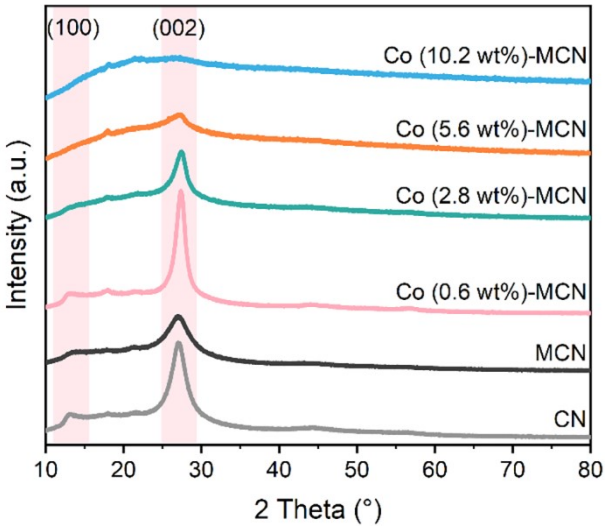

Fig. S9 XRD patterns of CN, MCN, Co (0.6 wt%)-MCN, Co (2.8 wt%)-MCN, Co (5.6 wt%)-MCN, and Co (10.2 wt%)-MCN.

The peaks featured at around 13° and 27° are assigned to the (100) and (002) facets of carbon nitride, corresponding to its in-plane order of tri-s-triazine units and interlayer stacking of conjugated heptazine units, respectively. The broadened and weakened characteristic peaks with a higher Co load indicate the lack of long-range order in the atomic arrangements of MCN in Co-MCN SACs.[24] Noted that there is another small peak at around 17°, which can be indexed to the (100) peak of the triazine phase of carbon nitride.[25,26]

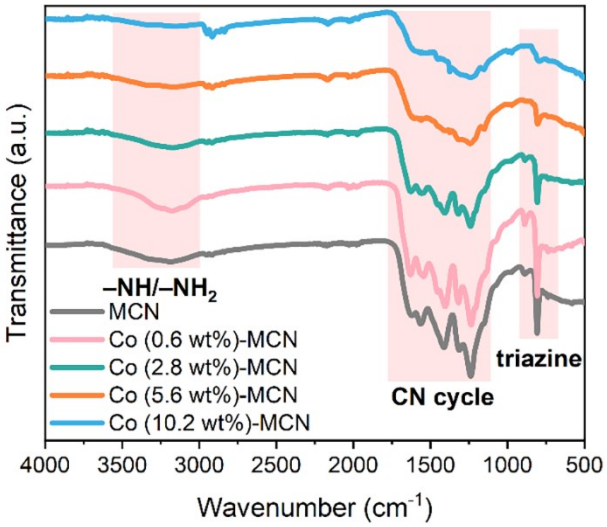

Fig. S10 FTIR spectra of CN, MCN, Co (0.6 wt%)-MCN, Co (2.8 wt%)-MCN, Co (5.6 wt%)-MCN, and Co (10.2 wt%)-MCN.

FTIR spectra show the surface functional groups of MCN and Co-MCN SACs. The gradually weakened –NH/–NH_2 bonds at 3000 - 3400 cm^{-1} with higher Co loads indicate the loss of these groups. Higher Co loads also decreased the intensity of the characteristic bands at 810 and 1200 - 1700 cm^{-1}, which were associated with the heptazine ring and the typical vibration modes of C–N heterocycles.

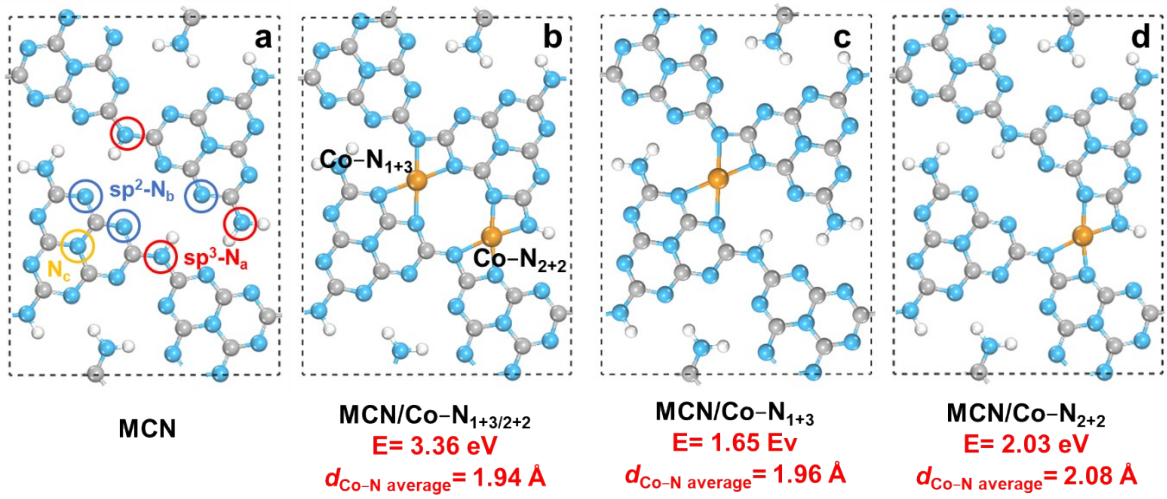

Fig. S11 Theoretical analysis of the molecular and coordination structures of (a) bulk CN, (b) MCN/Co−$N_{1+3/2+2}$, (c) MCN/Co−N_{1+3}, (d) MCN/Co−N_{2+2}. $d_{Co-N\ average}$ is the calculated average distance of Co−N bond in the models.

The molecular configurations of MCN, MCN/Co−N_{1+3}, MCN/Co−N_{2+2} and MCN/Co−$N_{1+3/2+2}$ were constructed based on the characterization results. All models were established based on hydrogen-bonded polymeric melon structures with NH/NH_2 groups.[20] The models were optimized by DFT calculations to avoid artificial biases. MCN consisting of H bond assembled melon chains with NH/NH_2 groups was configured according to the discussion on the thermal condensation of DCD. As illustrated in Figure S11a, there are three types of nitrogen in the MCN structure, i.e., amino groups/bridge nitrogen (sp^3-N_a), triangular edge nitrogen (sp^2-N_b) and central tertiary nitrogen (N_c).[27] MCN/Co−$N_{1+3/2+2}$ was constructed, considering the coexistence of Co−N_{1+3} and Co−N_{2+2} (Fig. S11b). For MCN/Co−N_{1+3}, Co atoms between the melon polymer chains can bond with one sp^3 N_a and two sp^2 N_b atoms by removing one H atom of MCN (Fig. S11c). For MCN/Co−N_{2+2}, Co atom can bond with two sp^3 N_a and two sp^2 N_b atoms on MCN (Fig. S11d). It is noted that the coexistence of Co−N_{1+3} and Co−N_{2+2} will facilitate the interaction of Co−N and improve the bonding strength. This leads to a shorter average bond distance of MCN/Co−$N_{1+3/2+2}$ than both MCN/Co−N_{1+3} and MCN/Co−N_{2+2}.

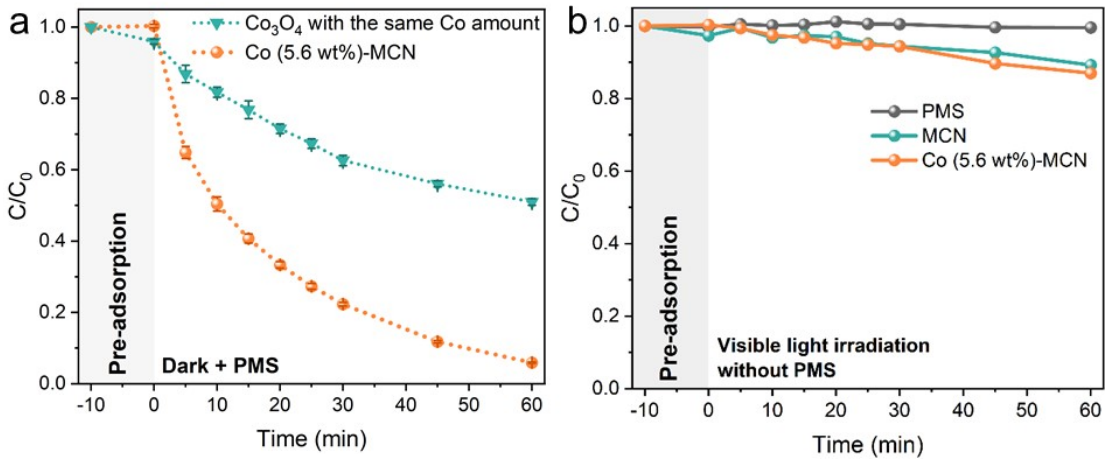

Fig. S12 (a) BPA degradation using Co_3O_4 with the same Co amount as Co (5.6 wt%)-MCN under dark condition. Reaction conditions: [BPA] = 10 mg L^{-1}, [PMS] = 0.5 mM, T = 25 °C, initial solution pH = 6.8. (b) BPA photodegradation performance without PMS addition. Reaction conditions: [BPA] = 10 mg L^{-1}, [PMS] = 0.5 mM if needed, [catalyst] = 0.2 g L^{-1}, T = 25 °C, initial solution pH = 6.8, 300 W Xeon lamp (> 420 nm) for visible light irradiation.

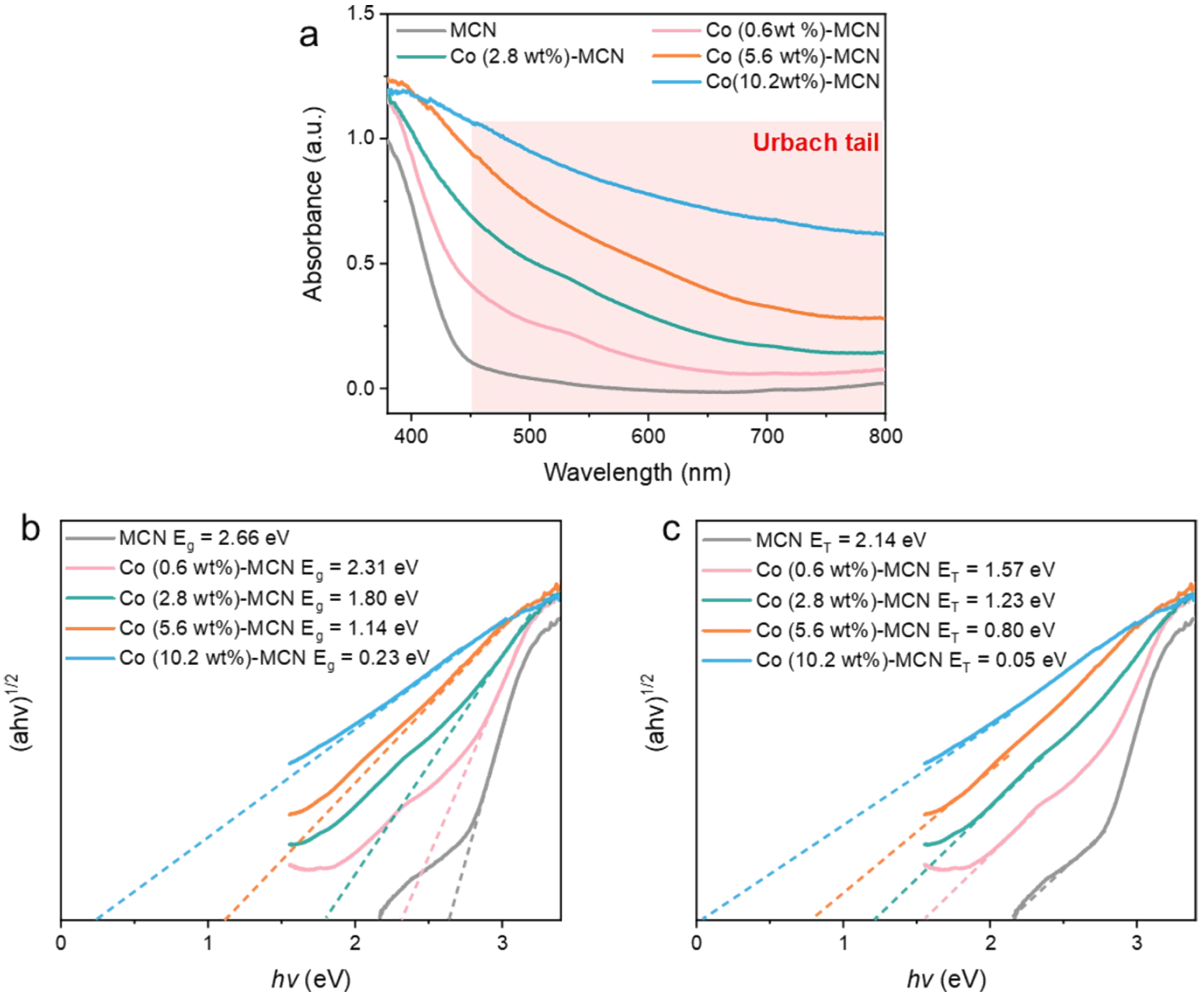

Fig. S13 (a) UV-Vis diffuse reflectance spectra, (b) Tauc plots and (c) transition energy of MCN, Co (0.6 wt%)-MCN, Co (2.8 wt%)-MCN, Co (5.6 wt%)-MCN, and Co (10.2 wt%)-MCN.

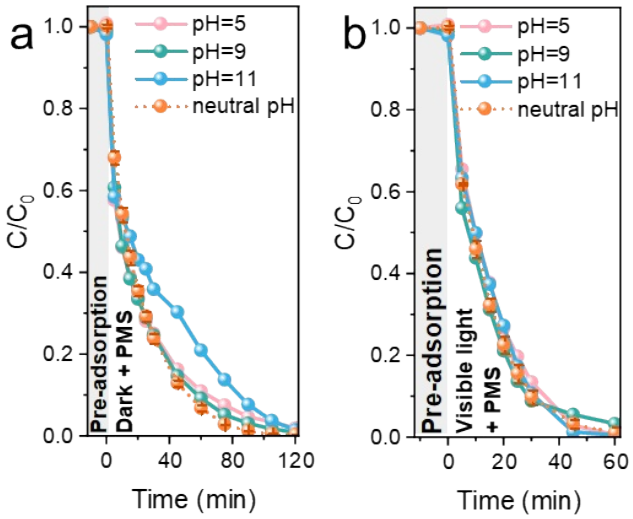

Fig. S14 Effect of the initial pH values (a) in dark and (b) under visible light irradiation on BPA degradation. Reaction conditions: [POP] = 10 mg L^{-1}, [PMS] = 0.5 mM, [catalyst] = 0.2 g L^{-1}, T = 25 °C. 300 W Xeon lamp (> 420 nm) was used for visible light irradiation.

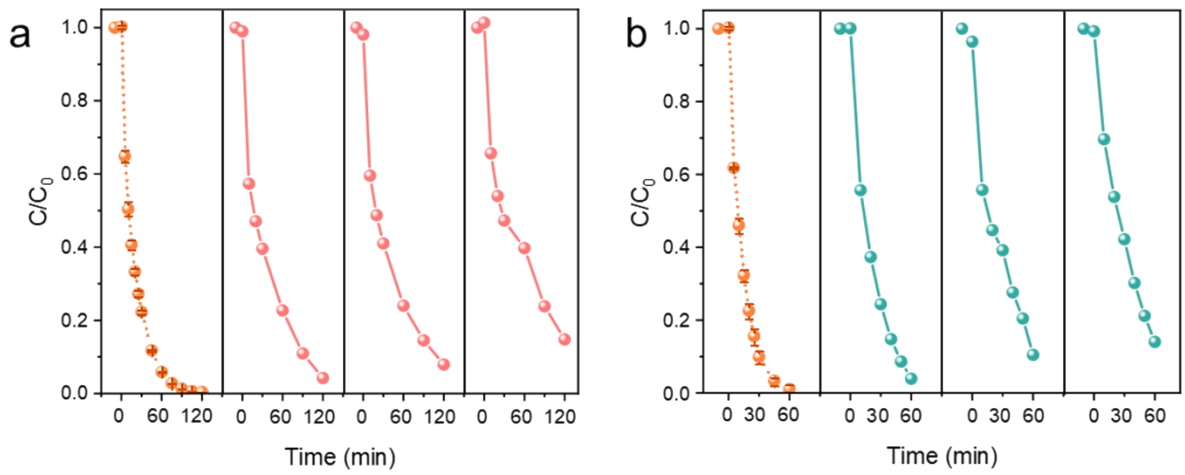

Fig. S15 Cycling tests (a) in dark and (b) under visible light irradiation. Reaction conditions: [BPA] = 10 mg L^{-1}, [PMS] = 0.5 mM, [catalyst] = 0.2 g L^{-1}, T = 25 °C, initial solution pH = 6.8, 300 W Xeon lamp (> 420 nm) for visible light irradiation.

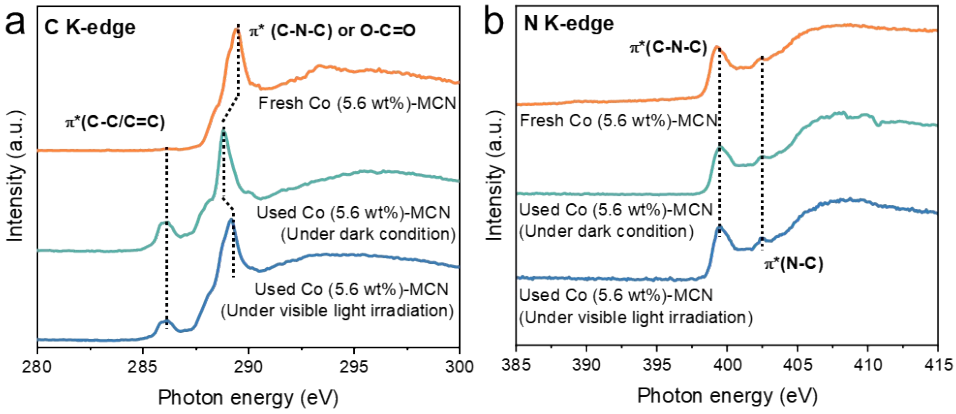

Fig. S16 XANES spectra of (a) C K-edge and (b) N K-edge of fresh Co (5.6 wt%)-MCN, used Co (5.6 wt%)-MCN (under dark condition) and used Co (5.6 wt%)-MCN (under visible light irradiation).

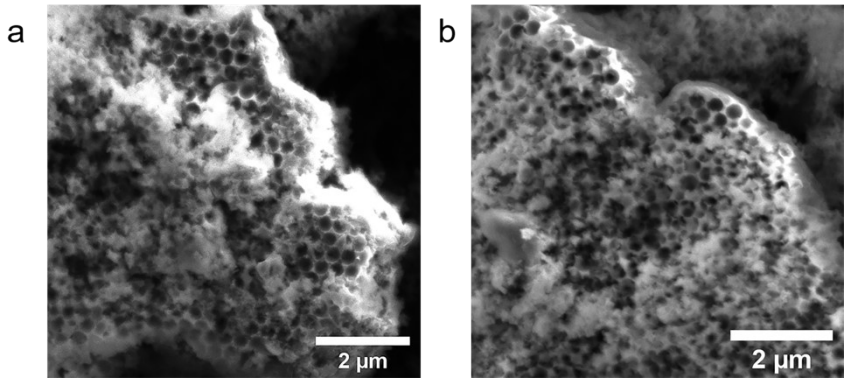

Fig. S17 SEM images of (a) used Co (5.6 wt%)-MCN (under dark condition) and (b) used Co (5.6 wt%)-MCN (under visible light irradiation) after 4 cycles catalytic PMS activation for BPA degradation.

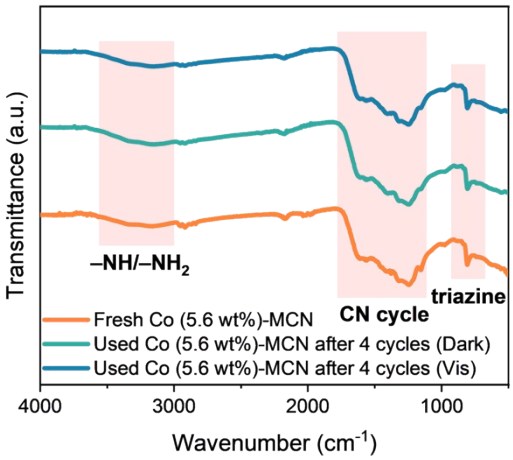

Fig. S18 FTIR spectra of fresh Co (5.6 wt%)-MCN, used Co (5.6 wt%)-MCN (under dark condition) and used Co (5.6 wt%)-MCN (under visible light irradiation) after 4 cycles catalytic PMS activation for BPA degradation.

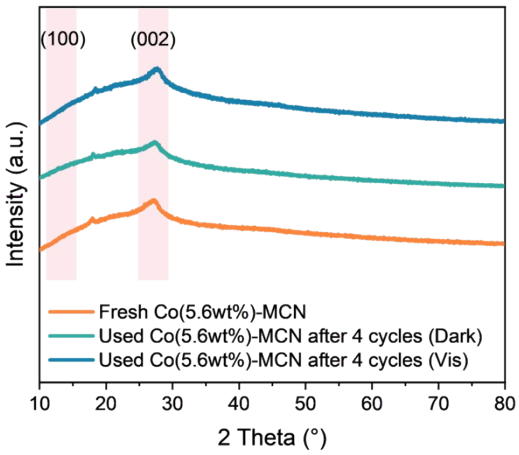

Fig. S19 XRD patterns of fresh Co (5.6 wt%)-MCN, used Co (5.6 wt%)-MCN (under dark condition) and used Co (5.6 wt%)-MCN (under visible light irradiation) after 4 cycles catalytic PMS activation for BPA degradation.

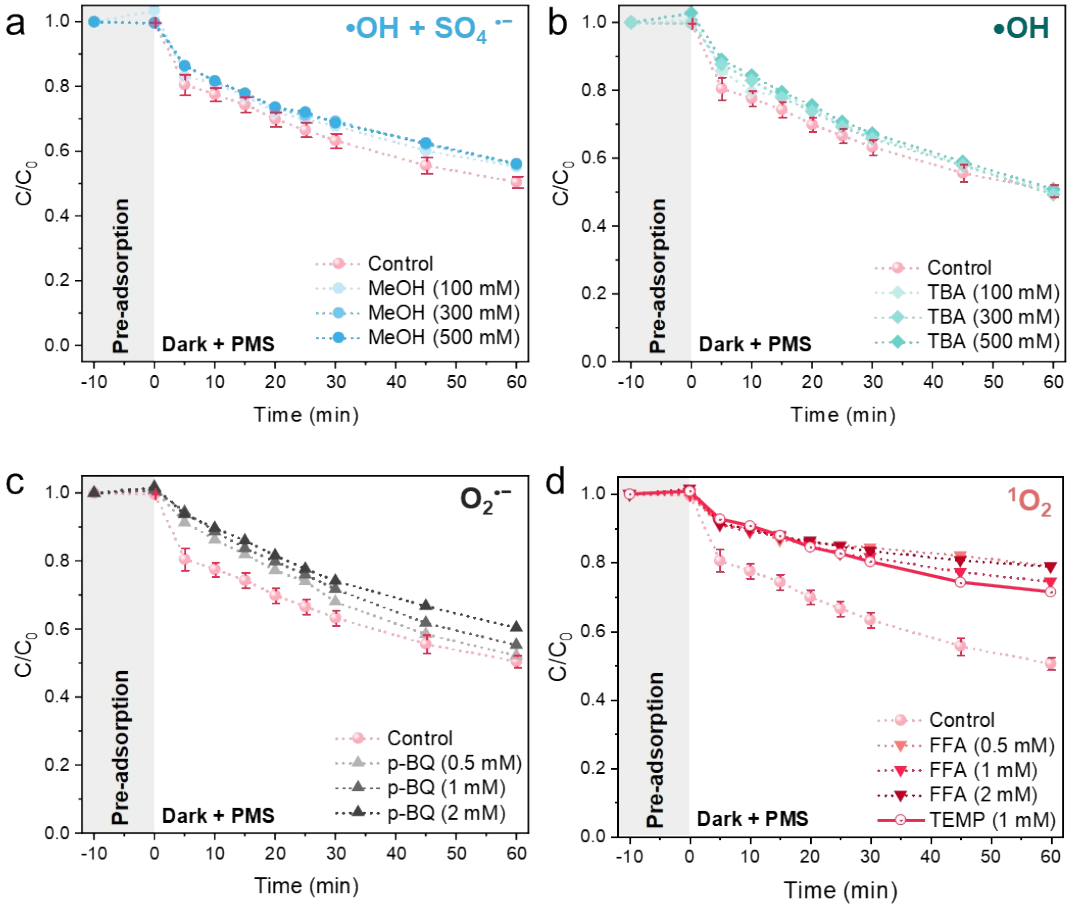

Fig. S20 Quenching study in dark of Co (0.6 wt%)-MCN with the presence of (a) MeOH, (b) TBA, (c) p-BQ, and (d) FFA and TEMP. Reaction conditions: [BPA] = 10 mg L^{-1}, [PMS] = 0.5 mM, [catalyst] = 0.2 g L^{-1}, T = 25 °C, initial solution pH = 6.8.

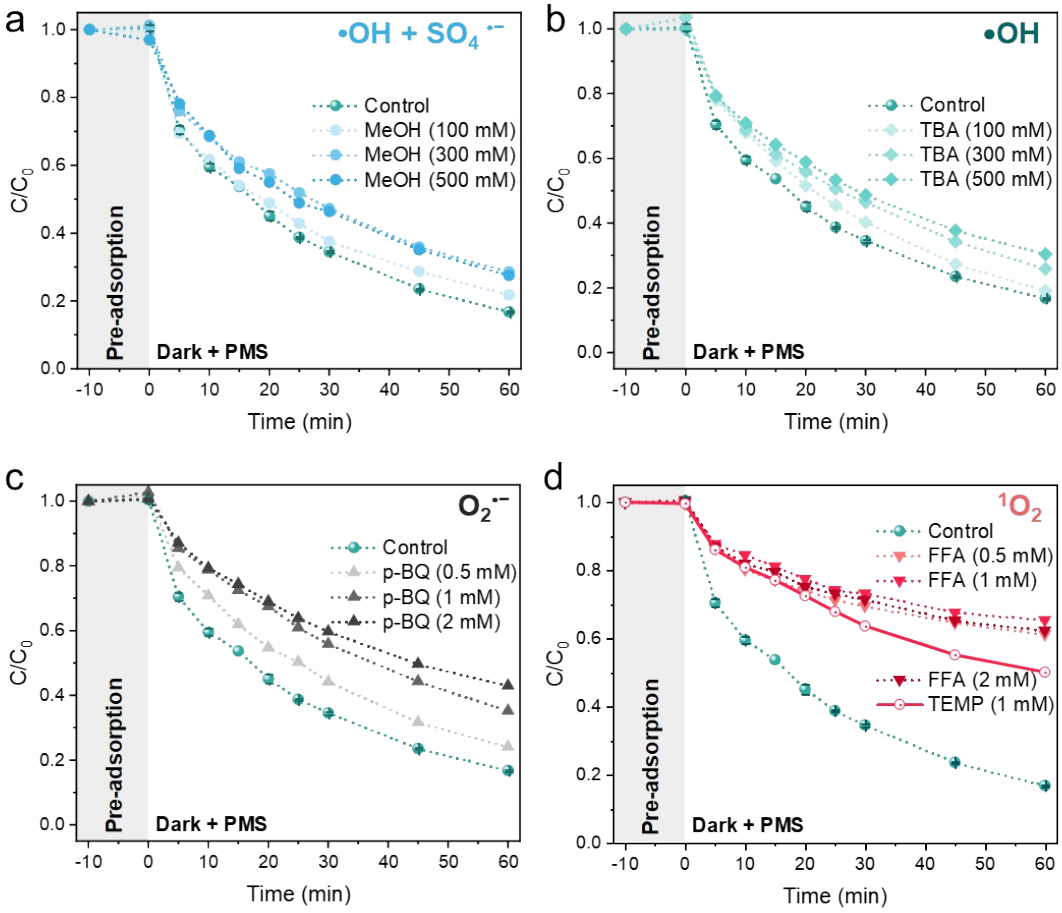

Fig. S21 Quenching study in dark of Co (2.8 wt%)-MCN with the presence of (a) MeOH, (b) TBA, (c) p-BQ, and (d) FFA and TEMP. Reaction conditions: [BPA] = 10 mg L^{-1}, [PMS] = 0.5 mM, [catalyst] = 0.2 g L^{-1}, T = 25 °C, initial solution pH = 6.8.

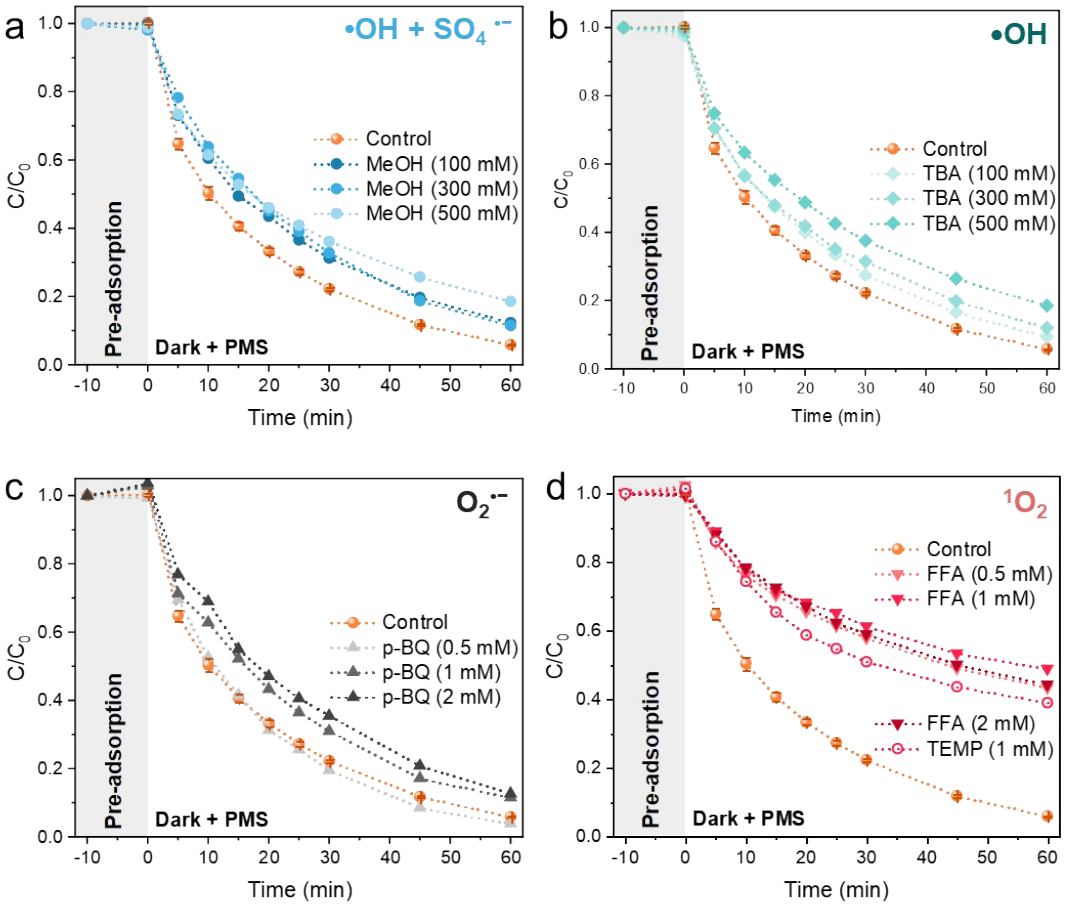

Fig. S22 Quenching study in dark of Co (5.6 wt%)-MCN with the presence of (a) MeOH, (b) TBA, (c) p-BQ, and (d) FFA and TEMP. Reaction conditions: [BPA] = 10 mg L^{-1}, [PMS] = 0.5 mM, [catalyst] = 0.2 g L^{-1}, T = 25 °C, initial solution pH = 6.8.

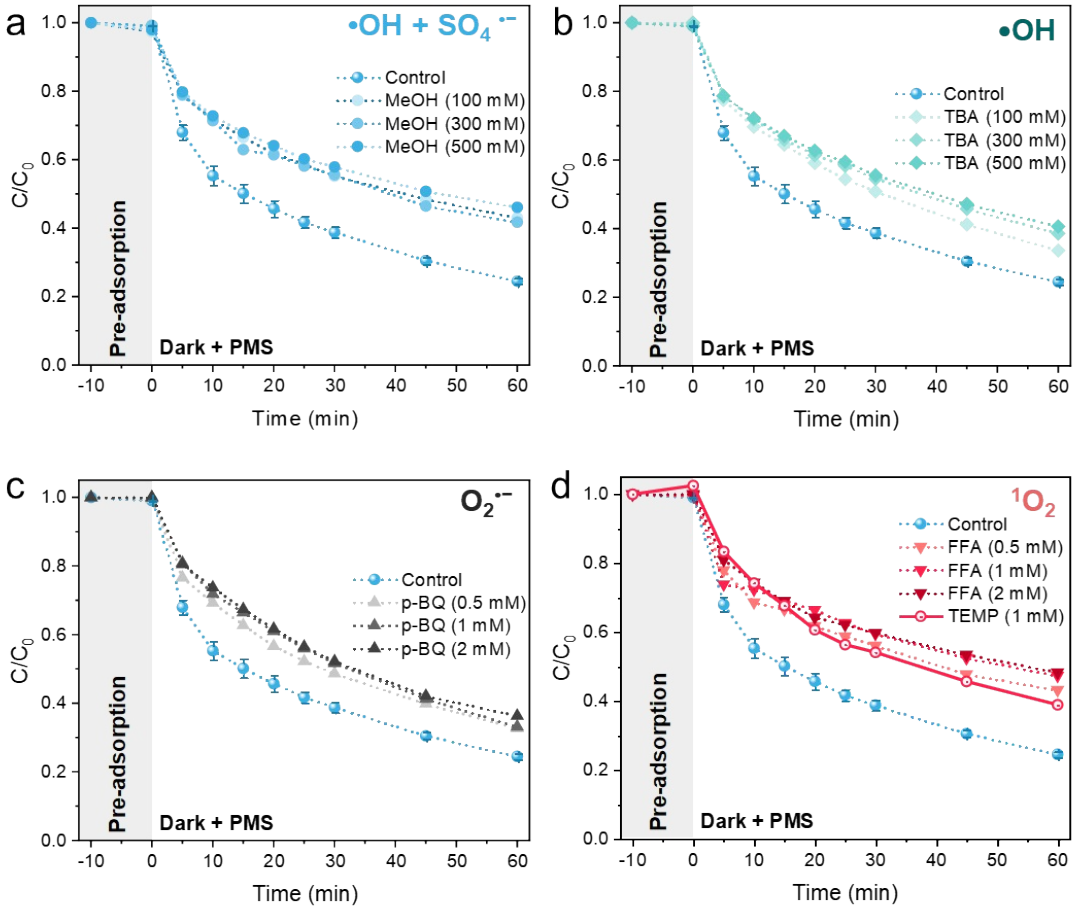

Fig. S23 Quenching study in dark of Co (10.2 wt%)-MCN with the presence of (a) MeOH, (b) TBA, (c) p-BQ, and (d) FFA and TEMP. Reaction conditions: [BPA] = 10 mg L^{-1}, [PMS] = 0.5 mM, [catalyst] = 0.2 g L^{-1}, T = 25 °C, initial solution pH = 6.8.

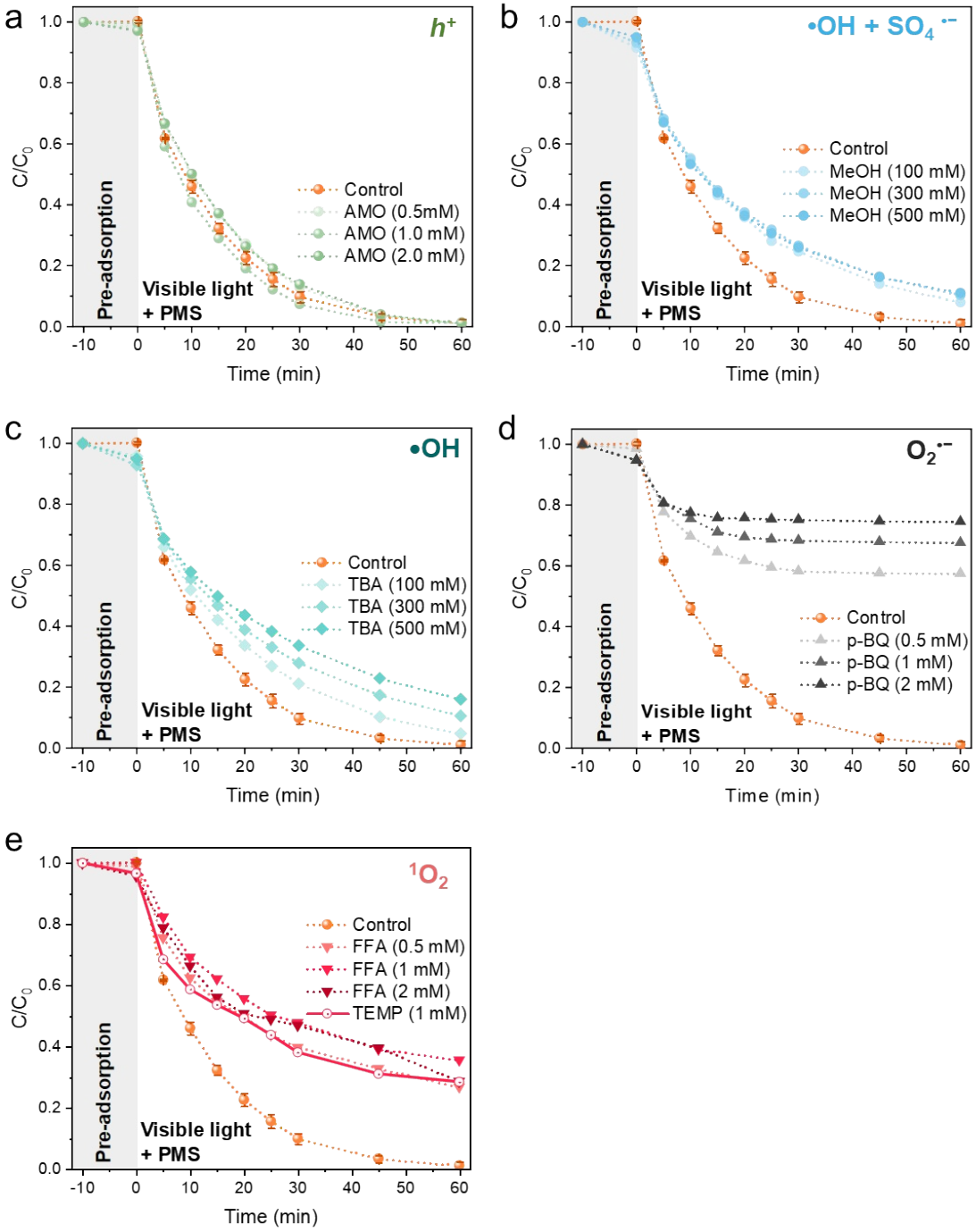

Fig. S24 Quenching study under visible light irradiation of Co (5.6 wt%)-MCN with the presence of (a) AMO, (b) MeOH, (c) TBA, (d) p-BQ and (e) FFA and TEMP. Reaction conditions: [BPA] = 10 mg L^{-1}, [PMS] = 0.5 mM, [catalyst] = 0.2 g L^{-1}, T = 25 °C, initial solution pH = 6.8, 300 W Xeon lamp (> 420 nm).

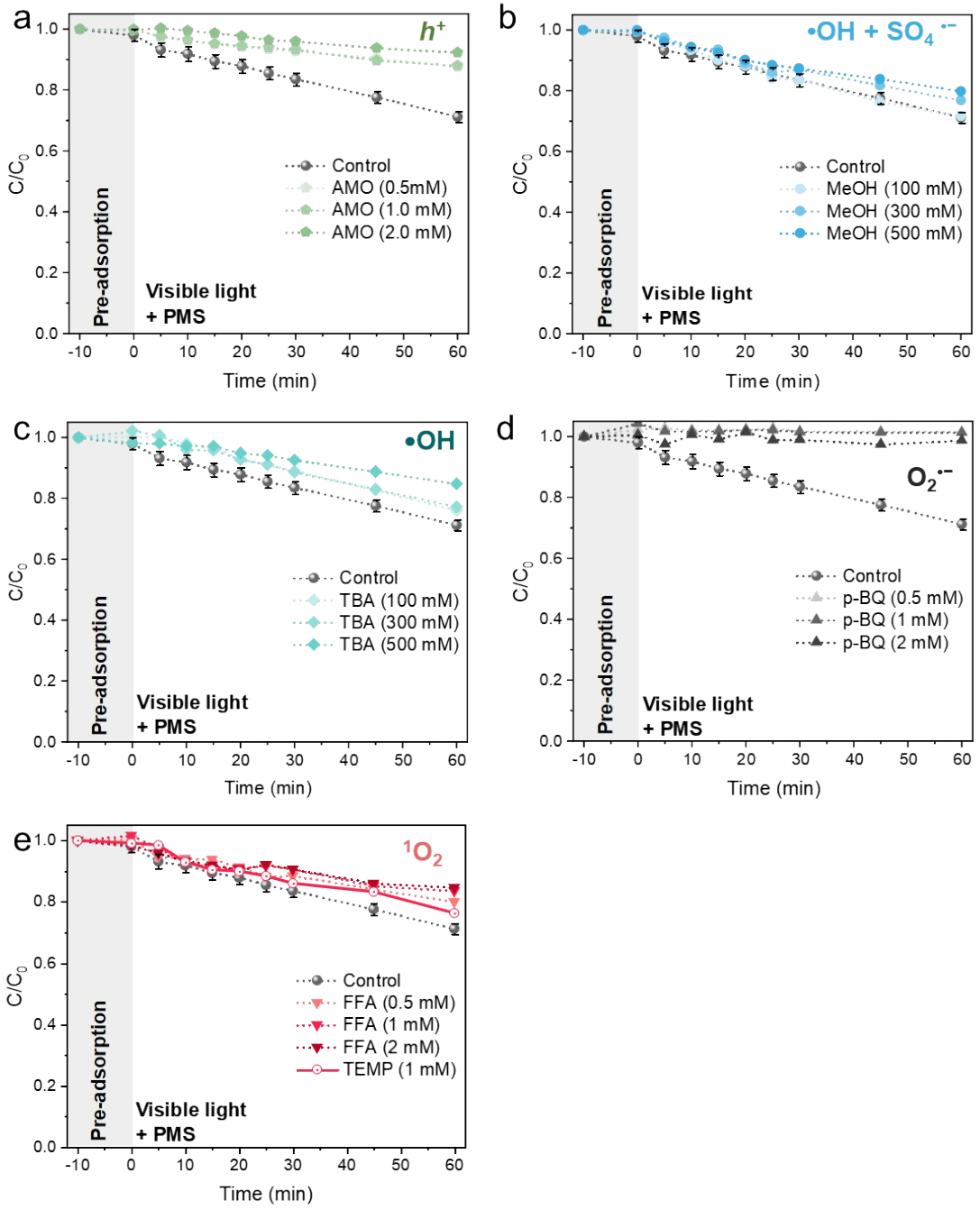

Fig. S25 Quenching study under visible light irradiation of MCN with the presence of (a) AMO, (b) MeOH, (c) TBA, (d) p-BQ, and (e) FFA and TEMP. Reaction conditions: [BPA] = 10 mg L^{-1}, [PMS] = 0.5 mM, [catalyst] = 0.2 g L^{-1}, T = 25 °C, initial solution pH = 6.8, 300 W Xeon lamp (> 420 nm).

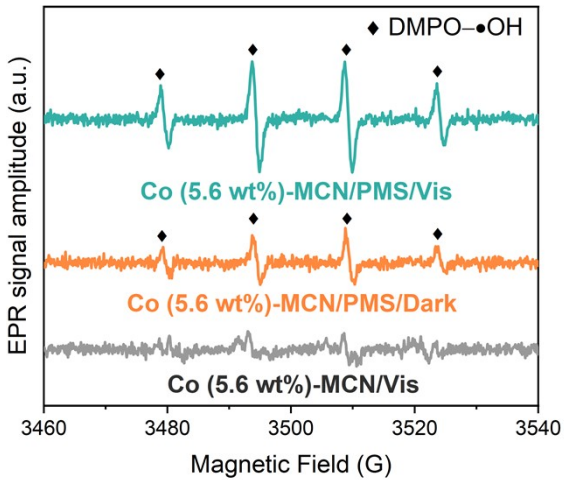

Fig. S26 EPR spectra of •OH. Reaction conditions: [PMS] = 0.5 mM, catalysts = 0.1 g/L, T= 25 °C.

DMPO spin-trapping ESR spectra demonstrated the existence of •OH radicals. It is also noted that no DMPO-$SO_4^{\bullet-}$ signal was detected, indicating the absence of $SO_4^{\bullet-}$. DMPO-$O_2^{\bullet-}$ was also captured in dark. The combination of quenching experiments and EPR results suggest that a small quantity of •OH, and $O_2^{\bullet-}$ were generated, but not directly involved in BPA degradation and could be *in situ* transformed into $^1O_2$ via Eq. S16.[28]

$$\bullet OH + {O_2}^{\bullet -} \rightarrow {}^1O_2 + OH^- \qquad Eq.S16$$

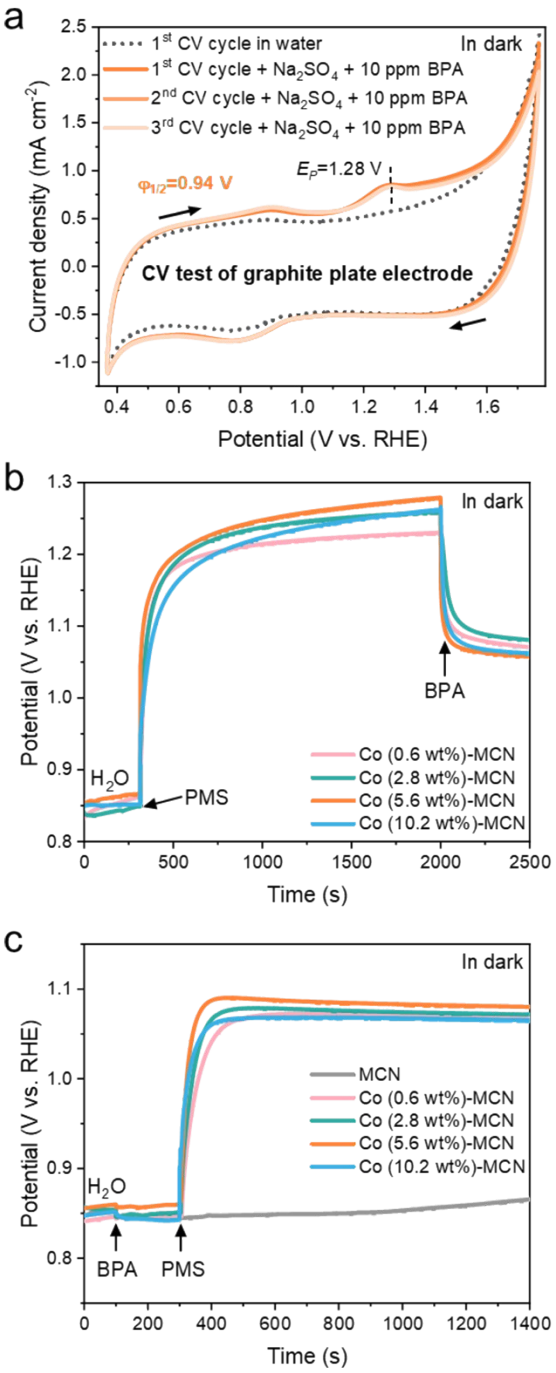

Fig. S27 Electron transfer in dark (a) CV curve of graphite plate electrode in 10 ppm BPA solution and 0.5M Na_2SO_4 as the electrolyte (scan rate: 10 mV s^{-1}, T = 25 °C). (b) Open-circuit potential measurements of different systems by adding PMS and then BPA. (c) Open-circuit potential measurements of different systems (Adding BPA and then PMS). Reaction conditions: [BPA] = 10 mg L^{-1}, [PMS] = 0.5 mM, T = 25 °C.

The half-wave potential ($\varphi_{1/2}$) for BPA oxidation was estimated to be 0.94 V by cyclic voltammetry (CV) (Fig. S27a). The value was then compared with the open-circuit potential (OCP) of Co-MCN SACs/PMS system in dark and light (Fig. S27b and 3g). After PMS

addition, the dramatically increased OCPs verified that Co-MCN SACs can contribute electrons to PMS, forming complexes of Co-MCN SACs/PMS* (1.23 – 1.27 V), which exceeded $\varphi_{1/2}$ of BPA, making them favorable to extract electrons from BPA via the oxidation process.[29,30] As evidenced, with BPA introduction after or before PMS addition (Fig. S27b and c), Co-MCN SACs/BPA/PMS* complexes showed lower OCPs of 1.07 – 1.09 V. In contrast, the OCP of MCN did not change much after PMS addition, which is below the $\varphi_{1/2}$ of BPA and the direct electron transfer oxidation process could not occur. Co (5.6 wt%)-MCN/PMS* complexes exhibited the highest OCP value, suggesting the most robust BPA oxidation capacity by electron transfer regime. The above OCP tests suggest that the electron transfer from Co-MCN SACs to PMS for PMS activation. This was also confirmed by the DFT simulation studies (Fig. 4b). The combination of both experimental and computational results suggests the PMS activation for $^1O_2$ generation will follow the pathway via $HSO_5 \rightarrow HSO_5^* \rightarrow {}^*OH + SO_4^* \rightarrow {}^*OH + SO_4^{2-} \rightarrow 2{}^*OH \rightarrow O^* \rightarrow 2O^* \rightarrow {}^*O{-}O^* \rightarrow {}^1O_2$.

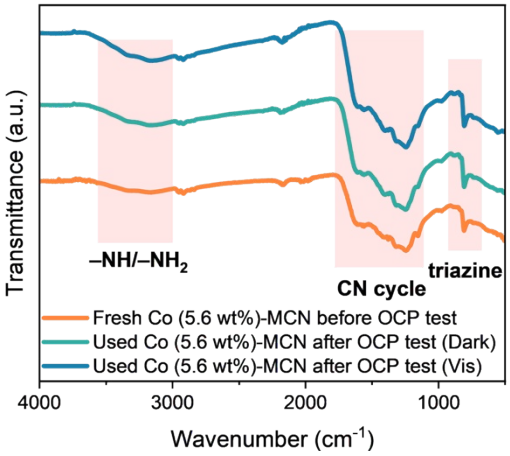

Fig. S28 FTIR spectra of fresh Co (5.6 wt%)-MCN, used Co (5.6 wt%)-MCN (under dark condition) and used Co (5.6 wt%)-MCN (under visible light irradiation) after Open-circuit potential measurements.

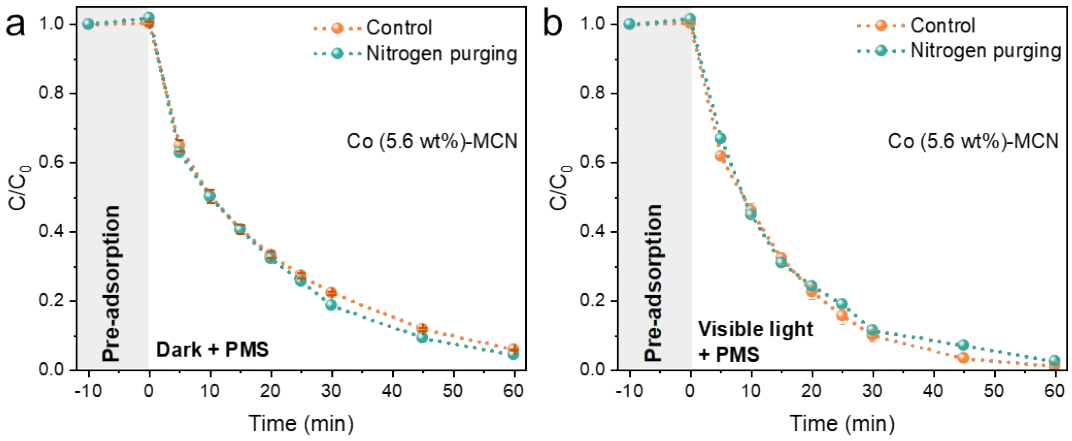

Fig. S29 Nitrogen gas purging to (a) Co (5.6 wt%)-MCN/PMS/dark and (b) Co (5.6 wt%)-MCN/PMS/visible light irradiation systems. Reaction conditions: [BPA] = 10 mg L^{-1}, [PMS] = 0.5 mM, [catalyst] = 0.2 g L^{-1}, T = 25 °C, initial solution pH = 6.8. 300 W Xeon lamp (> 420 nm) for visible light irradiation.

In principle, $O_2^{\bullet-}$ can be formed by one-electron reduction of dissolved O_2 in the solution (Eq. S17) or by PMS.[15,16,31,32] $^1O_2$ can be generated via the oxidation of $O_2^{\bullet-}$ by h^+ (Eq. S18),[33] so O_2 can be indirectly involved in $^1O_2$ generation.

$$O_2 + e^- \rightarrow O_2^{\bullet-} \qquad Eq.S17$$

$$O_2^{\bullet-} + h^+ \rightarrow {}^1O_2 \qquad Eq.S18$$

To reveal whether O_2 is participated in $O_2^{\bullet-}$ or $^1O_2$ generation in our systems, we conducted N_2 purging for 30 min to remove dissolved O_2 in Co (5.6 wt%)-MCN/PMS system. In order to eliminate the effect of gas produced from the reaction between catalysts and PMS, N_2 purging was continued during the degradation process under both dark and visible light irradiation conditions.

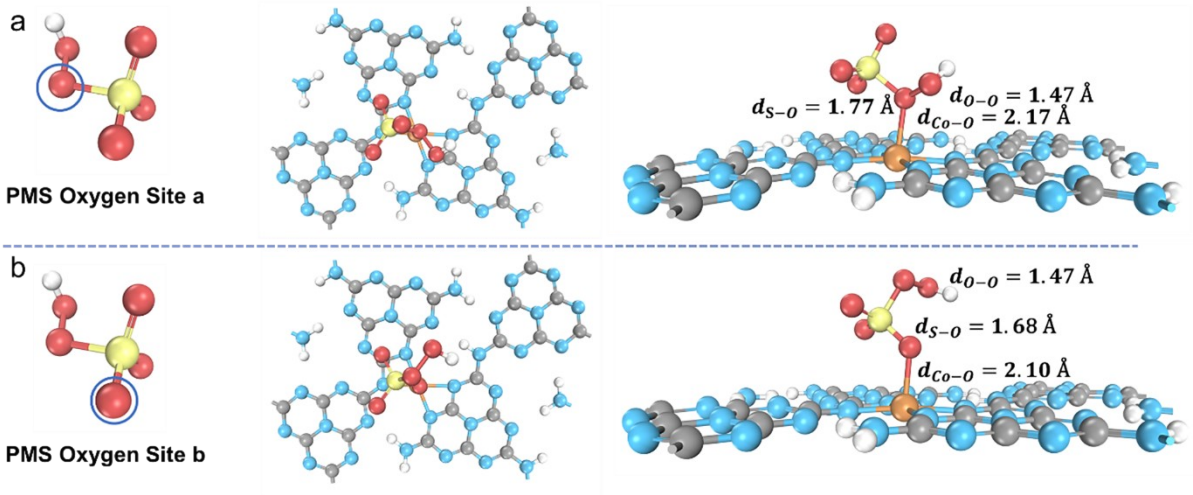

Fig. S30 PMS adsorption models at different oxygen sites using MCN/Co−N_{1+3} (a) at PMS oxygen site a; (b) at PMS oxygen site b.

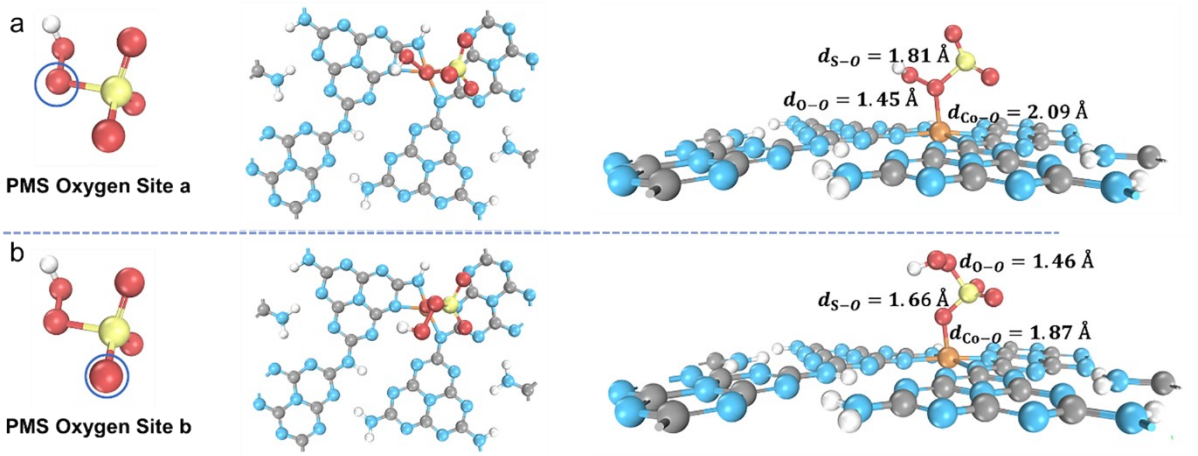

Fig. S31 PMS adsorption models at different oxygen sites using MCN/Co−N_{2+2} (a) at PMS oxygen site a; (b) at PMS oxygen site b.

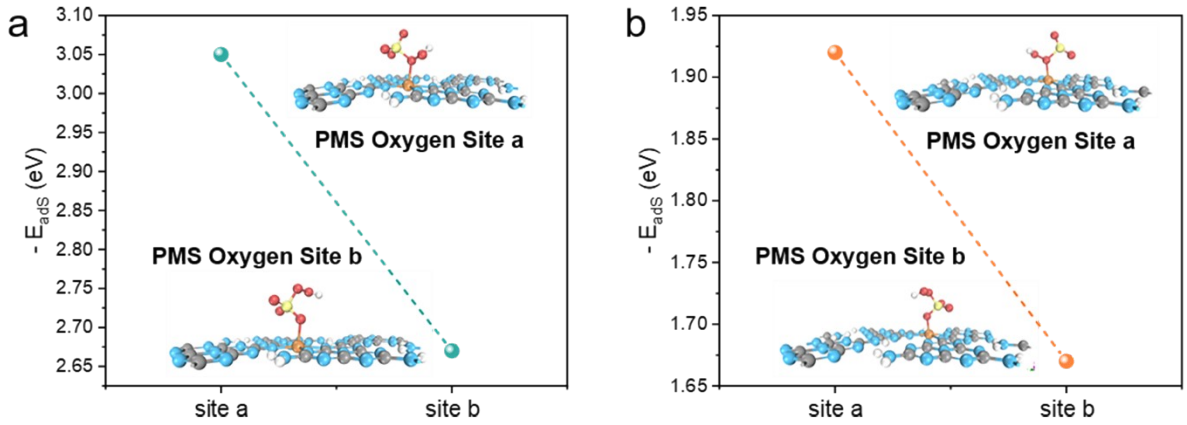

Fig. S32 Comparison of PMS adsorption energy at PMS oxygen sites 'a' and 'b' using (a) MCN/Co−N_{1+3} and (b) MCN/Co−N_{2+2}.

Single Co site was considered as the only chemical adsorption sites for PMS molecules. PMS molecules can only be physically adsorbed on C and N in the carbon nitride, which is weak (similar to PMS adsorption on MCN as shown in Fig. 4a). Based on previous studies, the adsorption of PMS (HSO_5) at 'oxygen site *b*' could drive the $^1O_2$ generation pathway via HSO_5 → HSO_5* → H*+SO_5* → SO_5* → 2SO_5* → $S_2O_8^{2-}$, SO_4^{2-} and $^1O_2$.[15,16] In this case, $^1O_2$ was produced during the loss of H atom and e^- from PMS to the catalyst. In comparison, the adsorption of PMS at 'oxygen site *a*' could drive the $^1O_2$ generation pathway via HSO_5 → HSO_5* → *OH + SO_4* → *OH + SO_4^{2-} → 2*OH → O* → 2O* → *O−O* → $^1O_2$. This is driven by the electron transfer from the catalyst to PMS and the subsequent reactions (Eqs. S3 - 9). For both MCN/Co−$N_{1+3/2+2}$ and MCN/Co−$N_{2+2/2+2}$, the adsorption energy ($|E_{ads}|$) at 'oxygen site *a*' is much higher than that at 'oxygen site *b*', suggesting that PMS prefers to be adsorbed at 'oxygen site *a*' and drives the second reaction route to produce $^1O_2$. This agrees well with our electrochemical measurements (Fig. 3g and S27b), where the electron transfer pathway is from the catalyst to PMS. Note that the adsorption of PMS at 'oxygen site *a*' can also drive the reaction for $O_2^{\bullet-}$ and •OH generation (Eqs. S11 - 14). These two reaction pathways were also driven by the electron transfer from the catalyst to PMS, confirmed by our electrochemical measurements (Fig. 3g and S27b).

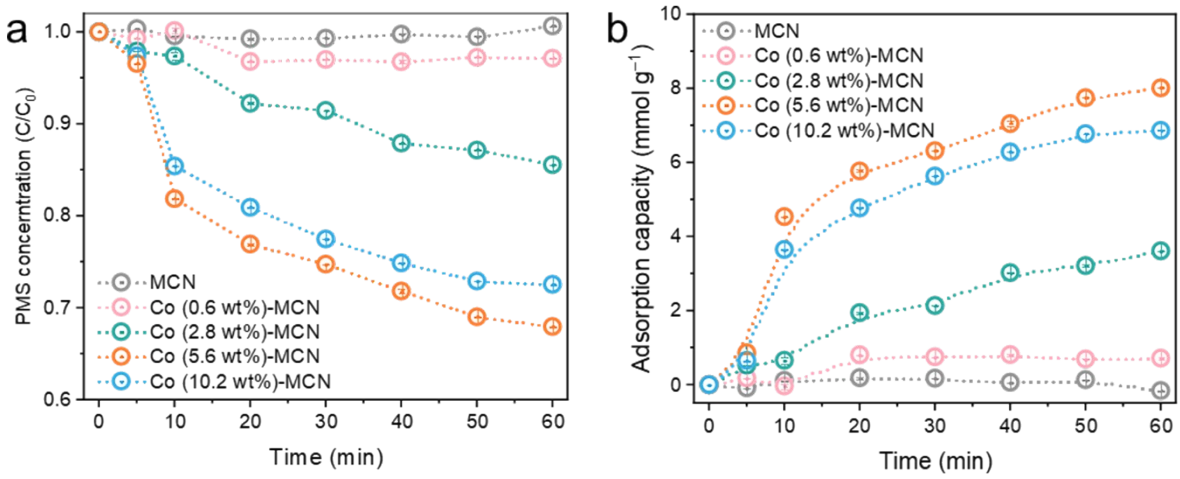

Fig. S33 Adsorption of PMS using different catalysts. (a) Reduction of PMS concentration, (b)PMS adsorption capacity. Reaction conditions: [BPA] = 10 mg L^{-1}, [PMS] = 0.5 mM, [catalyst] = 0.2 g L^{-1}, T = 25 °C, initial solution pH = 6.8. Experiments under darkness.

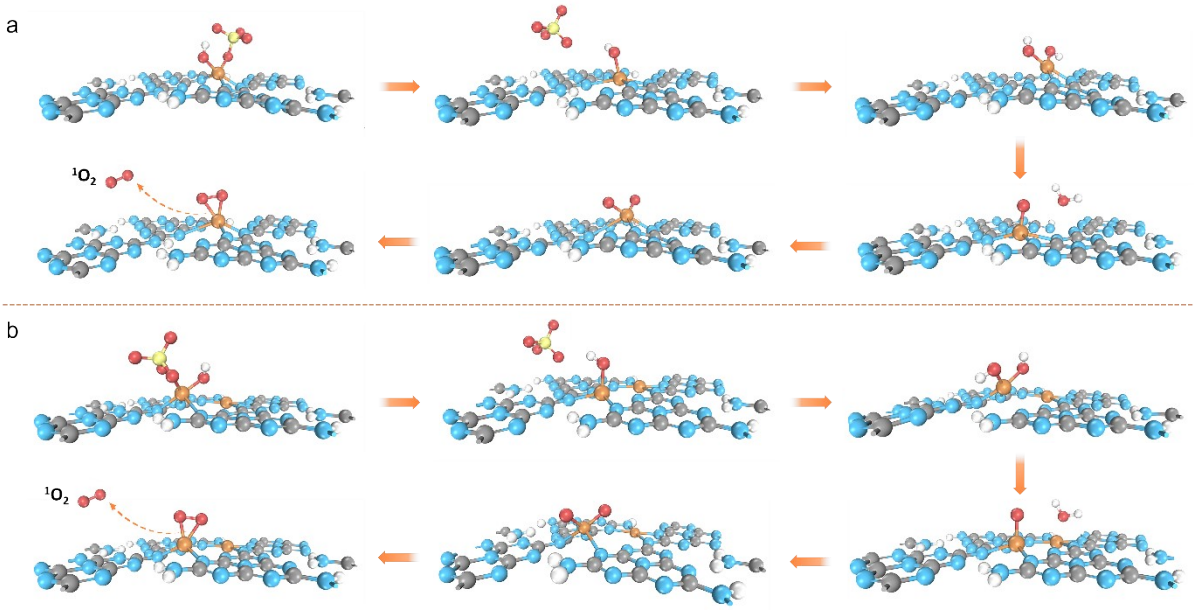

Fig. S34 Proposed reaction scheme with the intermediates having optimized geometry of (a) MCN/Co−N_{1+3} and (b) MCN/Co−$N_{1+3/2+2}$ towards $^1O_2$ generation pathway, based on the adsorption of intermediates at Co−N_{1+3} site.

As illustrated, $^1O_2$ generation proceeds by $HSO_5^- \rightarrow HSO_5^* \rightarrow *OH + SO_4^* \rightarrow *OH \rightarrow 2*OH \rightarrow O^* \rightarrow 2O^* \rightarrow *O{-}O^* \rightarrow {}^1O_2$. The dual-site adsorption of oxygen molecules at Co−N_4 site represents the formation of $^1O_2$ before desorption.

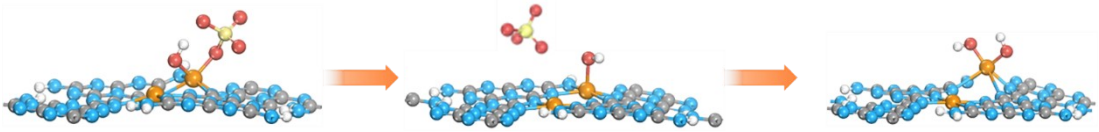

Fig. S35 Proposed reaction scheme with the intermediates (*OH and 2*OH) having optimized geometry of MCN/Co−$N_{1+3/2+2}$, based on the adsorption of intermediates at Co−N_{2+2} site.

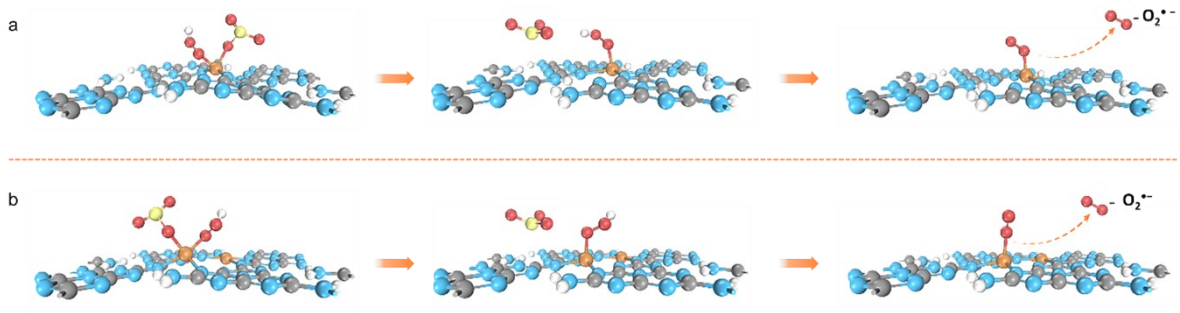

Fig. S36 Proposed reaction scheme with the intermediates having the optimized geometry of (a) MCN/Co−N_{1+3} and (b) MCN/Co−$N_{1+3/2+2}$ towards $O_2^{\bullet -}$ generation pathway, based on the adsorption of intermediates at Co−N_{1+3} site.

As illustrated, $O_2^{\bullet -}$ generation proceeds by $HSO_5^- \rightarrow HSO_5^* \rightarrow$ *OOH + $SO_3^* \rightarrow$ *OOH $\rightarrow$ OO* $\rightarrow O_2^{\bullet -}$. The single-site adsorption of oxygen molecules at Co−N_4 site represents the formation of $O_2^{\bullet -}$ before desorption.

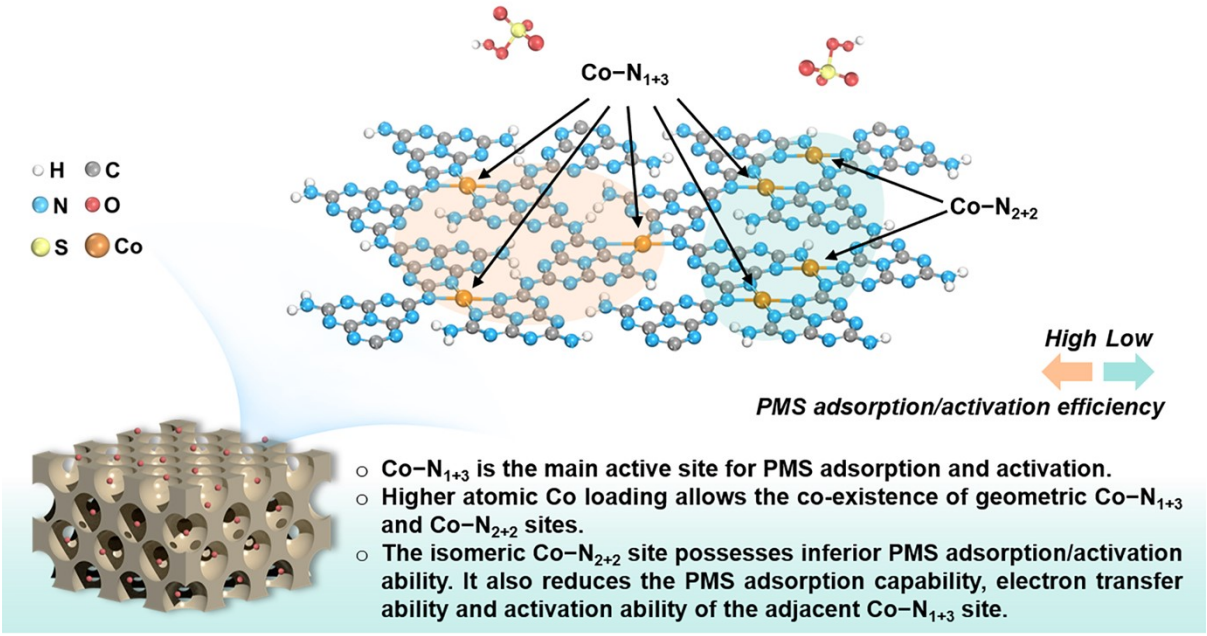

Scheme S1. Geometric Co−N_{1+3} and Co−N_{2+2} configurations in Co-MCN SACs for Fenton-like catalysis

3. Supplementary Tables

Table S1. Textural parameters and surface chemistry of CN, MCN and Co-MCN SACs.

	C/ at.%	N/ at.%	O/ at.%	Co/ at.%	SSA/ $m^2\ g^{-1}$	V_t/V_{meso} $cm^3\ g^{-1}$	Co/ wt. %
CN	46.4	48.93	4.67	-	4.6	0.05	-
MCN	48.16	46.42	5.42	-	27.2	0.15	-
Co (0.6 wt%)/MCN	43.91	53.19	2.73	0.16	34.8	0.19	0.6
Co (2.8 wt%)/MCN	50.04	45.82	3.85	0.29	32.1	0.19	2.8
Co (5.6 wt%)/MCN	54.47	39.73	5.43	0.37	16.1	0.11	5.6
Co (10.2 wt%)/MCN	67.85	27.38	4.36	0.41	10.4	0.06	10.2

The atomic ratio of elements was determined by the XPS analyses. SSA was calculated based on the Brunauer Emmett Teller (BET) method. Total pore volume (V_t) at $P/P_0 = 0.99$. Mesopore volume (V_{meso}) is supposed to be the same as V_t due to the micropore volume is negative. The Co weight percentage of Co-MCN SACs was determined by the thermogravimetric analysis (TGA).

Table S2. EXAFS fitting parameters at the Co K-edge for Co (5.6 wt%)-MCN.

Shell	C/N	R (Å)	δ^2 (10^{-3})	ΔE	R factor
Co−N1	0.8	1.8	8.6	8.5	0.006
Co−N2	1.0	2.0	4.7	9.1	
Co−N3	2.2	2.1	7.4	8.5	

CN: coordination numbers of identical atoms; *R*: interatomic distance; δ^2: Debye-Waller factors; Δ*E*: energy shift. *R* factor: goodness of fit. Error bounds that characterize the structural parameters obtained by EXAFS spectroscopy were estimated as C/N ± 20%; R ± 2%; ΔE ± 20%. EXAFS fitting results indicate that there exist three Co−N paths. Based on this, a MCN/Co−$N_{1+3/2+2}$ model was established. Isomeric Co−N_{1+3} and Co−N_{2+2} sites exist in a MCN/Co−$N_{1+3/2+2}$ structure, depending on the difference of coordinating sp hybridized N atoms (sp^3 N or sp^2 N atoms). The best-fit curve of MCN/Co−$N_{1+3/2+2}$ is shown in Fig. 1h.

Table S3. Co leaching from Co (5.6 wt%)-MCN after BPA degradation (from inductively coupled plasma mass spectrometry (ICP-MS))

Co leaching concertation in reaction solution (ppb)	Leaching amount of Co from Co (5.6 wt%)-MCN	Leaching percentage of Co from Co (5.6 wt%)-MCN
5.45 ppb	0.55 μg	0.05%

The result from ICP-MS suggests that there is almost no Co leaching (only 0.55 μg, 0.05%) from Co (5.6 wt%)-MCN after BPA removal process.

Table S4. Comparison with previous studies on CN-supported SACs

Single atom catalyst	Catalyst dose	PMS dose	Pollutants	Pollutants dose	Efficiency	Ref
CN supported Fe	0.5 g L^{-1}	1 mM	p-chlorophenol (4-CP)	0.1 mM	Dark: 100% in 10 min	34
Single atom Fe-dispersed g-C_3N_4 nanosheets	0.05 g L^{-1}	0.5 mM	sulfamethoxazole (SMX)	10 mg L^{-1}	Dark: 98.7% in 100% in 10 min	35
CoN/O-pCN	0.2 g L^{-1}	200 mg L^{-1}	Tetracycline (TC)	200 mg L^{-1}	Dark: 98.7 % in 60 min	36
Mn/O-PCN	0.3 g L^{-1}	1 mM	Enrofloxacin (ENR)	10 mg L^{-1}	Dark: 99 % in 20 min	37
Co-CN	0.5 g L^{-1}	1 mM	BPA	0.1 mM	Dark: 100% in 30 min; Visible light: 100% in 30 min	38
Ag modified mesoporous g-C_3N_4	0.1 g L^{-1}	1 mM	BPA	20 mg L^{-1}	Dark: 6% in 60 min, Visble light: 98% in 60 min	39
Co (5.6 wt%)-MCN	0.2 g L^{-1}	0.5 mM	BPA	10 mg L^{-1}	Dark: 94% in 60 min; Visible light: 99% in 60 min.	This work

References

1 G. Kresse and J. Hafner, *Phys. Rev. B*, 1994, **49**, 14251–14269.

2 G. Kresse and J. Furthmüller, *Comput. Mater. Sci.*, 1996, **6**, 15–50.

3 D. Joubert, *Phys. Rev. B - Condens. Matter Mater. Phys.*, 1999, **59**, 1758–1775.

4 G. Kresse and J. Hafner, *Phys. Rev. B*, 1993, **47**, 558–561.

5 J. P. Perdew, K. Burke and M. Ernzerhof, *Phys. Rev. Lett.*, 1996, **77**, 3865–3868.

6 B. Hammer, L. B. Hansen and J. K. Nørskov, *Phys. Rev. B - Condens. Matter Mater. Phys.*, 1999, **59**, 7413–7421.

7 P. E. Blöchl, *Phys. Rev. B*, 1994, **50**, 17953–17979.

8 K. Mathew, V. S. C. Kolluru, S. Mula, S. N. Steinmann and R. G. Hennig, *J. Chem. Phys.*, 2019, **151**, 235101.

9 K. Mathew, R. Sundararaman, K. Letchworth-Weaver, T. A. Arias and R. G. Hennig, *J. Chem. Phys.*, 2014, **140**, 0–8.

10 M. Methfessel and A. T. Paxton, *Phys. Rev. B*, 1989, **40**, 3616–3621.

11 S. Grimme, J. Antony, S. Ehrlich and H. Krieg, *J. Chem. Phys.*, **132**, 154104.

12 S. Grimme, S. Ehrlich and L. Goerigk, *J Comput Chem*, 2011, **32**, 1456–1465.

13 H. J. M. and J. D. Pack, *Phys. Rev. B*, 1976, **13**, 5188–5192.

14 X. Dong, Z. Chen, A. Tang, D. D. Dionysiou and H. Yang, *Adv. Funct. Mater.*, 2022, **32**, 2111565.

15 Z. Wang, E. Almatrafi, H. Wang, H. Qin, W. Wang, L. Du, S. Chen, G. Zeng and P. Xu, *Angew. Chem. Int. Ed.*, 2022, **134**, e202202338.

16 Y. Gao, T. Wu, C. Yang, C. Ma, Z. Zhao, Z. Wu, S. Cao, W. Geng, Y. Wang, Y. Yao, Y. Zhang and C. Cheng, *Angew. Chem. Int. Ed.*, 2021, **60**, 22513–22521.

17 W. Han, D. Li, M. Zhang, H. Ximin, X. Duan, S. Liu and S. Wang, *J. Hazard. Mater.*, 2020, **395**, 122695.

18 W. Stöber, A. Fink and E. Bohn, *J. Colloid Interface Sci.*, 1968, **26**, 62–69.

19 B. V. Lotsch, M. Döblinger, J. Sehnert, L. Seyfarth, J. Senker, O. Oeckler and W. Schnick, *Chem. - A Eur. J.*, 2007, **13**, 4969–4980.

20 P. Niu, L. Zhang, G. Liu and H. M. Cheng, *Adv. Funct. Mater.*, 2012, **22**, 4763–4770.

21 V. W. hei Lau and B. V. Lotsch, *Adv. Energy Mater.*, 2022, **12**, 2101078.

22 F. K. Kessler, Y. Zheng, D. Schwarz, C. Merschjann, W. Schnick, X. Wang and M. J. Bojdys, *Nat. Rev. Mater.*, 2017, **2**, 17030.

23 C. Lu, Y. Chen, Y. Yang and X. Chen, *Nano Lett.*, 2020, **20**, 5522–5530.

24 Y. Kang, Y. Yang, L. C. Yin, X. Kang, G. Liu and H. M. Cheng, *Adv. Mater.*, 2015, **27**, 4572–4577.

25 Z. Zeng, H. Yu, X. Quan, S. Chen and S. Zhang, *Appl. Catal. B Environ.*, 2018, **227**,

153–160.

26 L. Zhang, Z. Jin, H. Lu, T. Lin, S. Ruan, X. S. Zhao and Y. J. Zeng, *ACS Omega*, 2018, **3**, 15009–15017.

27 Y. Li, Y. Wang, C. L. Dong, Y. C. Huang, J. Chen, Z. Zhang, F. Meng, Q. Zhang, Y. Huangfu, D. Zhao, L. Gu and S. Shen, *Chem. Sci.*, 2021, **12**, 3633–3643.

28 J. Wang, B. Li, Y. Li, X. Fan, F. Zhang, G. Zhang and W. Peng, *Adv. Sci.*, 2021, **8**, 2101824.

29 W. Tian, J. Lin, H. Zhang, X. Duan, H. Wang, H. Sun and S. Wang, *J. Hazard. Mater.*, 2022, **423**, 127083.

30 W. Ren, C. Cheng, P. Shao, X. Luo, H. Zhang, S. Wang and X. Duan, *Environ. Sci. Technol.*, 2022, **56**, 78–97.

31 J. Lin, W. Tian, Z. Guan, H. Zhang, X. Duan, H. Wang, H. Sun, Y. Fang, Y. Huang and S. Wang, *Adv. Funct. Mater.*, 2022, **32**, 2201743.

32 W. Tian, J. Lin, H. Zhang, X. Duan, H. Sun, H. Wang and S. Wang, *J. Hazard. Mater.*, 2021, **408**, 124459.

33 Y. Yang, G. Zeng, D. Huang, C. Zhang, D. He, C. Zhou, W. Wang, W. Xiong, B. Song, H. Yi, S. Ye and X. Ren, *Small*, 2020, **16**, 2001634.

34 L. S. Zhang, X. H. Jiang, Z. A. Zhong, L. Tian, Q. Sun, Y. T. Cui, X. Lu, J. P. Zou and S. L. Luo, *Angew. Chem. Int. Ed.*, 2021, **60**, 21751–21755.

35 G. Zhao, W. Li, H. Zhang, W. Wang and Y. Ren, *Chem. Eng. J.*, 2022, **430**, 132937.

36 X. Liu, D. Huang, C. Lai, L. Qin, S. Liu, M. Zhang and Y. Fu, *J. Colloid Interface Sci.*, 2023, **629**, 417–427.

37 C. He, W. Xia, C. Zhou, D. Huang, C. Zhang, B. Song, Y. Yang, J. Li, X. Xu, Y. Shang and L. Du, *Chem. Eng. J.*, 2022, **430**, 132751.

38 B. Liu, W. Guo, Q. Si, W. Jia, S. Zheng, H. Wang, Q. Zhao, H. Luo, J. Jiang and N. Ren, *Chem. Eng. J.*, 2022, **446**, 137277.

39 Y. Wang, X. Zhao, D. Cao, Y. Wang and Y. Zhu, *Appl. Catal. B Environ.*, 2017, **211**, 79–88.